

CONDENSED  
MATTER

## Electronic Structure of Magnetic Topological Insulators $\text{Mn}(\text{Bi}_{1-x}\text{Sb}_x)_2\text{Te}_4$ with Various Concentration of Sb Atoms

D. A. Glazkova<sup>a, \*</sup>, D. A. Estyunin<sup>a</sup>, I. I. Klimovskikh<sup>a, b</sup>, T. P. Makarova<sup>a</sup>, O. E. Tereshchenko<sup>c, d, e</sup>,  
K. A. Kokh<sup>e, f, g</sup>, V. A. Golyashov<sup>c, d, e</sup>, A. V. Koroleva<sup>a</sup>, and A. M. Shikin<sup>a</sup>

<sup>a</sup> St. Petersburg State University, St. Petersburg, 198504 Russia

<sup>b</sup> National University of Science and Technology MISiS, Moscow, 119049 Russia

<sup>c</sup> Rzhanov Institute of Semiconductor Physics, Siberian Branch, Russian Academy of Sciences, Novosibirsk, 630090 Russia

<sup>d</sup> Shared Access Center SKIF, Boreskov Institute of Catalysis, Siberian Branch, Russian Academy of Sciences,  
Novosibirsk, 630559 Russia

<sup>e</sup> Novosibirsk State University, Novosibirsk, 630090 Russia

<sup>f</sup> Sobolev Institute of Geology and Mineralogy, Siberian Branch, Russian Academy of Sciences, Novosibirsk, 630090 Russia

<sup>g</sup> Kemerovo State University, Kemerovo, 650000 Russia

\*e-mail: [daria.a.glazkova@gmail.com](mailto:daria.a.glazkova@gmail.com)

Received February 3, 2022; revised February 3, 2022; accepted February 3, 2022

Intrinsic magnetic topological insulator  $\text{MnBi}_2\text{Te}_4$  provides a promising platform to implement the quantum anomalous Hall effect at increased temperatures and other unique topological effects. However, to do this, the energy gap opening at the Dirac point should be located at the Fermi level. One of the widely used methods to shift the Dirac point toward the Fermi level is the partial substitution of Bi atoms for Sb atoms. In this work, the electronic structure of the core levels and valence band of  $\text{Mn}(\text{Bi}_{1-x}\text{Sb}_x)_2\text{Te}_4$  compounds with various concentration  $x$  of Sb atoms from 0 to 1 has been studied. It has been shown that the Dirac point with an increase in the concentration of Sb atoms is shifted toward the Fermi level and becomes localized at it when  $x \approx 0.3$ . In this case, the “rigid” shift of the valence band, including the Mn 3*d* level, has been observed without changes in the structure of the valence and conduction bands. The concentration dependence of the shift of the Dirac point is approximated by a square root function, which corresponds to a linear increase in the charge carrier density.

DOI: 10.1134/S0021364022100083

A great amount of attention has recently been paid to studies of magnetic topological insulators (TIs) because they have a unique combination of topological and magnetic properties. This combination of properties makes it possible to implement many theoretically predicted effects such as the quantum anomalous Hall effect, the axion insulator state, the topological superconducting state, and the Weyl semimetal state [1–8]. However, to form such states, it is necessary to introduce magnetism in TIs, which are initially nonmagnetic materials, in order to open a energy gap in the electronic structure of topological surface states at the Dirac point.

The first methods of introducing magnetism in TIs were based on doping of TIs with magnetic impurities or on the proximity effect in magnetic heterostructures [9–15]. An increase in the concentration of magnetic impurities increases both the exchange interaction and the energy gap at the Dirac point, but the concentration of defects often simultaneously increases, the quality of a sample is worsened, and the

mobility of electrons decreases [12]. As a result, many quantum effects, including the quantum anomalous Hall effect, which occur in magnetically doped TIs, are observed only at extremely low temperatures 0.1–1 K [11].

The discovery of intrinsic stoichiometric magnetic TI  $\text{MnBi}_2\text{Te}_4$  allows one to avoid such an increase in defectiveness because this material includes magnetic atoms as an intrinsic layer [16]. This made it possible to increase the energy gap opened at the Dirac point, as well as to significantly increase the temperature of the quantum anomalous Hall effect [17], which approaches the magnetic transition temperature (the temperature of the quantum anomalous Hall effect for doped TIs is several orders of magnitude lower than the magnetic transition temperature).

$\text{MnBi}_2\text{Te}_4$  single crystals are characterized by strong electron doping: the Dirac point is located at a binding energy of 0.25–0.28 eV and the Fermi level is located in the conduction band [16–20]. However, for the quantum anomalous Hall effect to occur, the

Dirac point and the corresponding energy gap should be localized at the Fermi level. One of the well-known and widely used methods for the energy shift of the Dirac cone for  $\text{Bi}_2\text{Te}_3$ -based TIs [21] is the replacement of some Bi atoms by Sb atoms, which introduce the hole type of conduction in TIs. The  $(\text{Bi}_{1-x}\text{Sb}_x)_2\text{Te}_3$  compound retains its topological properties in the entire range of dopant concentrations  $x$  from 0 to 1. As the concentration of Sb atoms increases, the type of charge carriers in the TI changes to holes and the Dirac point is shifted toward the Fermi level. At a certain  $x$  value, transition occurs from the  $n$  doping type to the  $p$  doping type through the charge neutral point. The charge carrier density in magnetic TIs with fractional stoichiometry  $\text{Mn}(\text{Bi}_{1-x}\text{Sb}_x)_2\text{Te}_4$  varies similarly under the substitution of Bi atoms for Sb atoms [22–24].

It was revealed that fractional stoichiometry is also responsible for other changes. The magnetic structure [22] and transport properties of a material change, and the Néel temperature decreases [23]. It was shown that the energy gap in topological state can change [24]. There is no commonly accepted concentration of Sb at which the Dirac point is at the Fermi level [22–27]. The authors of [23] found that the necessary concentration of Sb atoms can depend on the method and details of the synthesis of the samples under study.

In this work, we study in detail the dependence of the electronic structure of core levels and the valence and conduction bands of bulk crystals with fractional stoichiometry  $\text{Mn}(\text{Bi}_{1-x}\text{Sb}_x)_2\text{Te}_4$  on the concentration of Sb atoms in the entire  $x$  range from 0 to 1. The structure of the valence band and the core levels were measured by means of angle-resolved photoemission spectroscopy (ARPES) and X-ray photoelectron spectroscopy (XPS) with use of synchrotron radiation. The measurements of core levels and the valence band were performed at the same point and under the same conditions. A certain correlation between the stoichiometry of the sample and the energy shift of the Dirac point under the variation of the concentration of Sb atoms was obtained.

## EXPERIMENTAL RESULTS AND DISCUSSION

In this work, we studied a series of samples with stoichiometry  $\text{Mn}(\text{Bi}_{1-x}\text{Sb}_x)_2\text{Te}_4$  under the variation of the concentration of Sb atoms  $x = 0, 0.1, 0.2, 0.3, 0.4, 0.5$ , and 1 introduced at growth.

The samples were grown by the Bridgman method for which some inhomogeneity of stoichiometry over the volume is possible. Thus, for detailed characterization of the sample (concentrations of Sb, Bi, Te, and Mn and the position of the Dirac point), photoemission measurements for each sample at different energies of photons were carried out at the same point (see the section Methods).

The structural quality of the samples was tested by low-energy electron diffraction (LEED). Figure 1a shows the LEED pattern recorded at an energy of electrons of 75 eV for the  $\text{Mn}(\text{Bi}_{0.6}\text{Sb}_{0.4})_2\text{Te}_4$  sample. The LEED pattern is characterized by the hexagonal arrangement of reflections. Blue lines in Fig. 1a mark the unit cell in the reciprocal space. Such LEED patterns are characteristic of materials with the crystal structure  $R\bar{3}m$  inherent in  $\text{Mn}(\text{Bi}_{1-x}\text{Sb}_x)_2\text{Te}_4$  compounds. Such LEED patterns were observed for all studied samples, which indicates that the crystal structure is the same, and the sharpness of observed reflections confirms a high quality of the prepared samples.

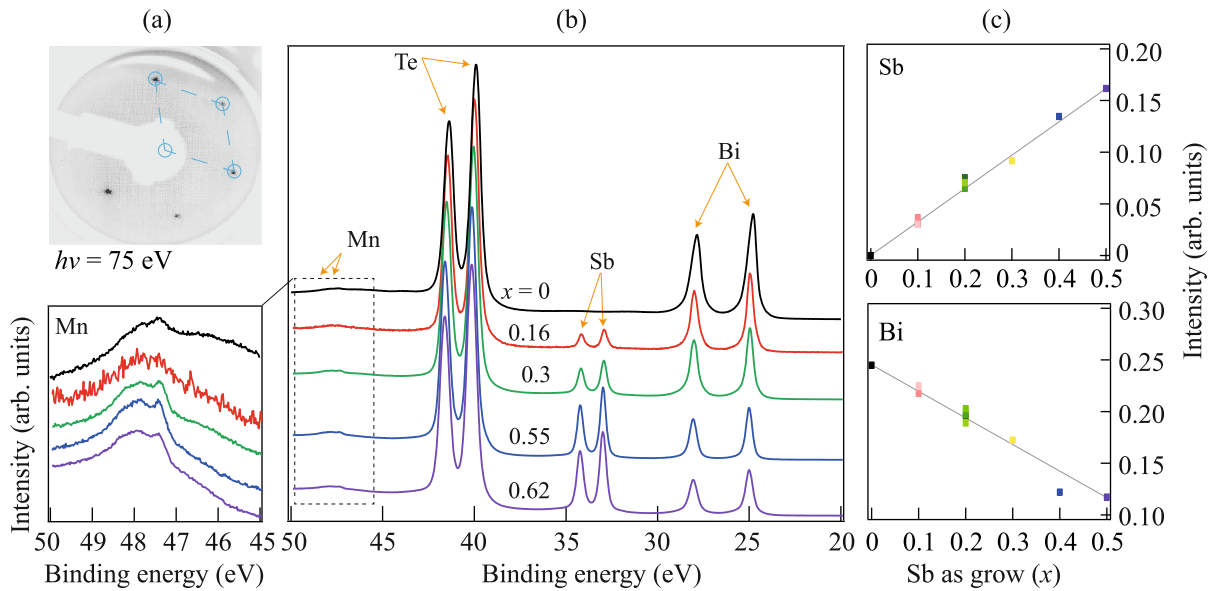
To study the dependence of the electronic structure of  $\text{Mn}(\text{Bi}_{1-x}\text{Sb}_x)_2\text{Te}_4$  samples on the doping level with Sb atoms, we used XPS and ARPES simultaneously.

Figure 1b shows the XPS spectra of core levels for samples with various concentrations of Sb atoms in the binding energy range of 20–50 eV, which includes doublet of peaks of Bi  $5d$ , Sb  $4d$ , Te  $4d$ , and Mn  $3p$  core levels, i.e., all elements that are present in the sample. The concentration of Sb atoms (and other elements) in the samples for studied regions was calculated from these spectra. The resulting concentrations of Sb atoms are given above the corresponding spectra. It is seen that an increase in the concentration of Sb atoms results in a smooth decrease in the intensity of the Bi peak and in an increase in the intensity of the Sb peak.

The bottom left panel of Fig. 1b shows the spectra of the Mn  $3p$  line for various concentrations of Sb. It is seen that both the intensity of the peak and its shape vary insignificantly for all stoichiometries of the studied samples, which indicates that the concentration of Mn atoms in the samples under study is approximately constant and, indirectly, that the magnetic properties of the material are stable.

Figure 1c shows the dependence of the relative XPS intensities of the (top) Sb and (bottom) Bi peaks on the concentration of Sb atoms introduced in grown samples. Different colors correspond to different samples. The relative normalization of the peak intensities is such that the sum of the intensities of the presented Bi  $5d$ , Sb  $4d$ , Te  $4d$ , and Mn  $3p$  peaks is 1. As seen, the relative intensity of the Sb peak increases linearly with some spread for different samples, which confirms the expected linear increase in the fraction of Sb in stoichiometry. The bottom part of Fig. 1c demonstrates that the relative intensity of the Bi peak decreases linearly.

To estimate the concentrations of atoms from the intensities of the corresponding peaks in XPS spectra (at certain points of the sample), we used the database of photoionization cross sections for core levels from [28]. The analysis with this database gave  $x \sim 0.16$  instead of 0.1,  $x \sim 0.3$  instead of 0.2,  $x \sim 0.38$  instead of



**Fig. 1.** (Color online) (a) LEED pattern with the hexagonal arrangement of reflections characteristic of all  $\text{Mn}(\text{Bi}_{1-x}\text{Sb}_x)_2\text{Te}_4$  samples. Blue dashed lines indicate a unit cell. (b) XPS spectra measured at  $h\nu = 120$  eV for  $\text{Mn}(\text{Bi}_{1-x}\text{Sb}_x)_2\text{Te}_4$  samples with various concentrations of Sb atoms. The structure of the Mn  $3p$  levels is shown in the bottom left panel. (c) Relative XPS intensities of the Sb (top panel) and Bi peaks (bottom panel) versus the concentration of Sb atoms in grown samples. Different colors correspond to different samples.

0.3,  $x \sim 0.55$  instead of 0.4, and  $x \sim 0.62$  instead of 0.5. As seen, the measured concentrations are larger than values introduced at the growth of all samples under study.

The excess of the calculated concentration of Sb atoms over the value introduced at growth was mentioned in [29]. This excess can be due to the feature of growth and the feature of the estimate. The crystal was grown from a solvent based on  $(\text{Bi}, \text{Sb})_2\text{Te}_3$  rather from the melt. Thus, the chemical analysis indicates that Sb predominantly enters the crystal with respect to the solvent. The analysis of samples from different parts of the ingot shows that the Bi/Sb ratio holds in the process of crystallization of  $\text{Mn}(\text{Bi}_{1-x}\text{Sb}_x)_2\text{Te}_4$ . In turn, the estimate of concentrations depends on the used databases.

To determine changes in the doping level of  $\text{Mn}(\text{Bi}_{1-x}\text{Sb}_x)_2\text{Te}_4$  samples and the shift of the Dirac point with respect to the Fermi level under the variation of the concentration of Sb atoms, ARPES spectra of the valence and conduction bands were measured in the range close to the Fermi level. These spectra for various estimated concentrations of Sb atoms (at the same points of the sample) are shown in Figs. 2a–2h. The bulk valence band (BVB), the bulk conduction band (BCB), the fundamental gap between them, where a part of the Dirac cone is located (the remaining part is mixed with the bulk valence and bulk conduction bands), and the energy gap opened at the Dirac point are indicated in Fig. 2a. The valence band is also marked in all figures by the blue line. As the

concentration of Sb atoms increases, the Dirac point is shifted toward the Fermi level and crosses it at  $x \approx 0.3$ . The blue dashed lines indicate the positions of the Dirac point. Spectra for concentrations exceeding  $x = 0.3$  demonstrate only the valence band; consequently, the position of the Dirac point can be explicitly determined only for samples with  $x = 0, 0.16, 0.24,$  and  $0.3$ .

To determine the positions of the Dirac point for  $x > 0.3$ , we assume that the details of the electronic structure for various  $x$  values are identical and spectra of the sample with  $x = 0.16$  are overlaid in Figs. 2e–2h above the Fermi level with the corresponding shift (shown semitransparent, black-and-white). The spectrum for  $x = 0.24$  was obtained at another setup and at a different energy of photons exciting photoemission, but it fits the same dependence.

The dependence of the estimated positions of the Dirac point in various samples  $\text{Mn}(\text{Bi}_{1-x}\text{Sb}_x)_2\text{Te}_4$  on the concentration of Sb atoms  $x$  calculated from the intensities of core levels is shown in Fig. 3a (left axis). It is seen in Fig. 3a that the experimental points can be well approximated by the function  $f(x) \sim \sqrt{x}$  shown by the dashed line. The wave vector at the Fermi level is related to the density of states at the Fermi level for states of the Dirac cone as [21]

$$\frac{Dk_f^2}{4\pi} = |n_{ss}|. \quad (1)$$

Here,  $D$  is the degeneracy of the Dirac fermion (constant) and  $|n_{ss}|$  is the charge carrier density on the

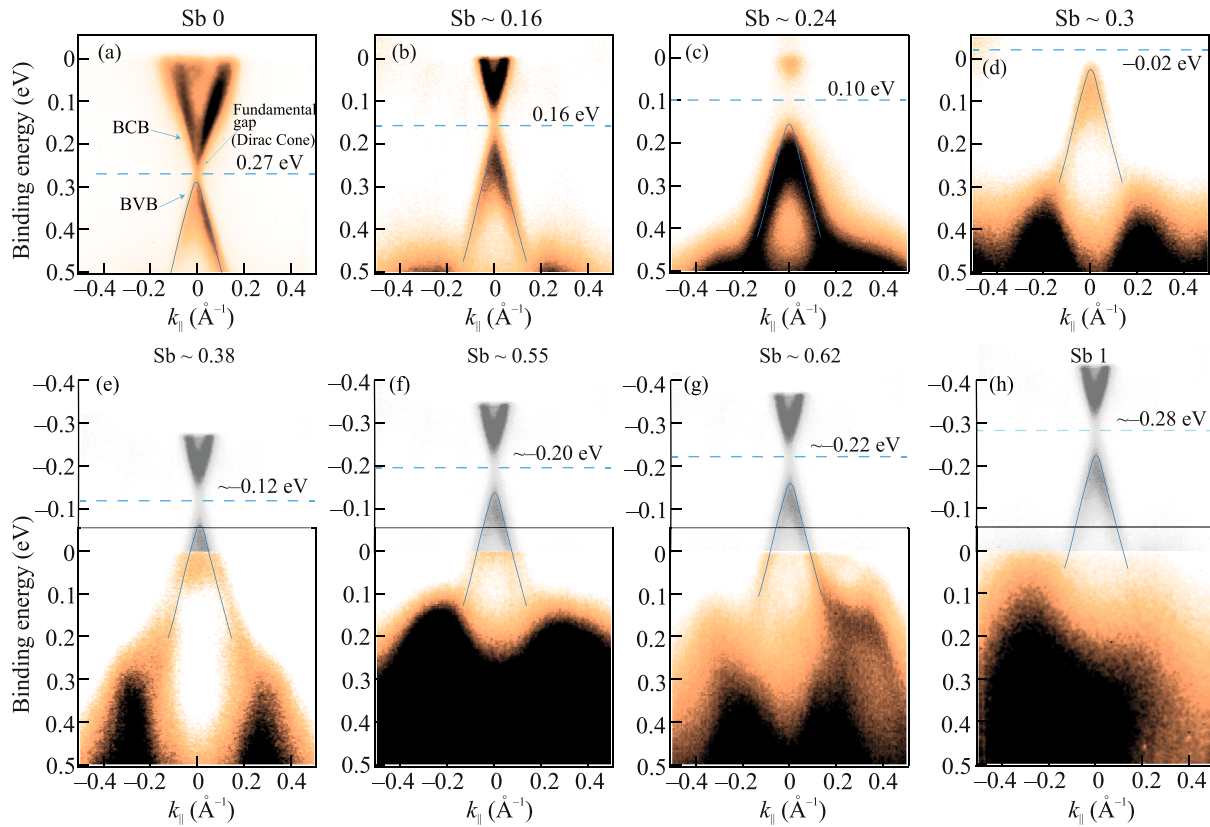


**Fig. 2.** (Color online) Structure of valence and conduction states and the position of the Dirac point at various concentrations of Sb atoms. The position of the Dirac point at concentrations above  $x = 0.3$  is estimated by overlaying the spectrum measured at the concentration  $x = 0.16$  (semitransparent black-and-white). The position of the Dirac point is marked by the horizontal blue dashed straight line.

surface. In the case of the linear dispersion of Dirac electrons, the wave vector at the Fermi level is proportional to the position of the Dirac point. Good square root approximation of the experimental points indicates that topological states without contributions from states of the valence and conduction bands are located at the Fermi level when the concentration of Sb atoms is near  $x = 0.3$ . Such a dependence of the Dirac point on the concentration of Sb atoms was observed for the  $\text{Bi}_2\text{Te}_3$  [30],  $\text{MnBi}_2\text{Te}_4$  [23], and  $\text{MnBi}_6\text{Te}_{10}$  [31] samples.

It is noteworthy that the positions of points at the ends of the dependence deviate from the square root approximation, which can be due to the contribution from states of the conduction or valence band to the density of states at the Fermi level. In addition, it is difficult to estimate the position of the Dirac point for pure  $\text{MnSb}_2\text{Te}_4$  by the used method because of the large energy spacing between the Dirac point and Fermi level.

It was observed in our study that the Dirac point crosses the Fermi level at the concentration of Sb  $x \sim 0.3$ . This is in agreement with some other studies performed by various methods [22, 23]. However, the

authors of [23, 25–27] observed the transition through the Fermi level at different concentrations of Sb atoms. This difference can be due to features in the used methods of growth of samples and the corresponding concentrations of defects. This was partially confirmed in [23], where it was found that the energy spacing between the Fermi level and Dirac point for thin films is smaller than that for bulk samples.

To analyze the shift of the valence band, which is not directly related to the shift of the Dirac cone, we studied the energy shift of the Mn  $3d$  peak localized in the region of the valence band. Figure 3b shows the measured energy shift of the Mn  $3d$  peak under the variation of the concentration of Sb atoms. Spectra for different concentrations of Sb atoms are given in different colors and are normalized to the height of the Mn  $3d$  peak.

To separate the Mn  $3d$  peak in the valence band, we used resonant photoelectron spectroscopy with an energy of 50 eV corresponding to the Mn  $3p$ – $3d$  transition [32].

The binding energy positions of the Mn  $3d$  peak are given by blue circles in Fig. 3a (right axis). The left axis step in Fig. 3a coincides with the right axis step. Thus,

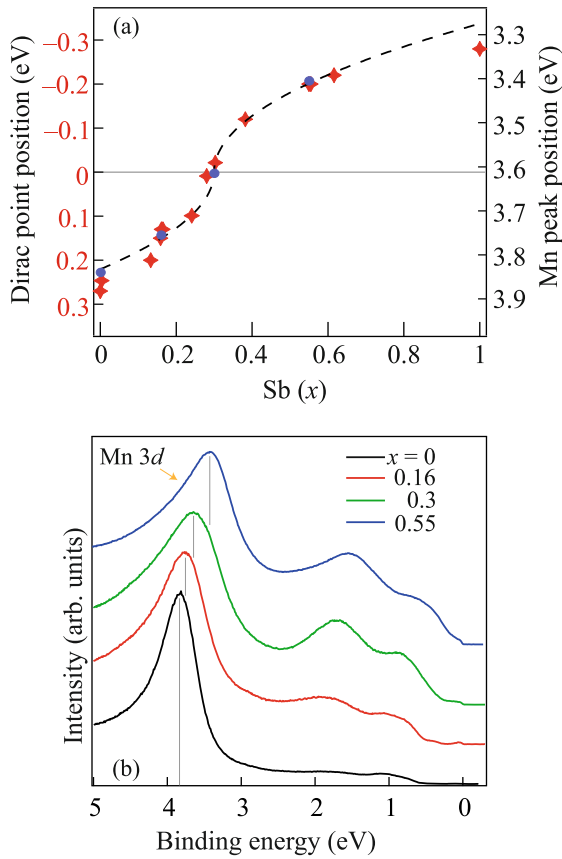


**Fig. 3.** (Color online) (a) (Left axis, red points) Dirac point energy and (right axis, blue circles) Mn 3d peak position for  $\text{Mn}(\text{Bi}_{1-x}\text{Sb}_x)_2\text{Te}_4$  versus the concentration of Sb atoms. (b) Measured electron density of states at the  $\Gamma$  point (in the range  $k_{\parallel} = \pm 0.5 \text{ \AA}^{-1}$ ) in resonant photoelectron spectra ( $h\nu = 50 \text{ eV}$ ) with the Mn 3d peak contour at various concentrations of Sb atoms.

it is clearly seen that the energy shift of the Mn 3d peak coincides with the energy shift of the Dirac point. This confirms that estimate of the Dirac point is valid under the condition that the valence band is rigidly shifted.

An increase in the concentration of Sb atoms results in a decrease in the intensity of the resonant Mn 3d peak with respect to the valence band. On the one hand, this can be attributed to a decrease in the intensity of magnetic resonance (and the total magnetic properties) for  $\text{Mn}(\text{Bi}_{1-x}\text{Sb}_x)_2\text{Te}_4$  compounds with increasing  $x$ . On the other hand, the presented data allow us to assume that, since the shift of the valence band is approximately twice as large as the shift of core levels, the energy spacing between the levels involved in resonance changes and the energy position of the resonance is shifted. The measurement at a photon energy of 50 eV already gives the result on the descending part of the resonance peak at the energy spacing from the maximum increasing with the concentration of Sb.

## CONCLUSIONS

To summarize, we have analyzed changes in the structure of the valence and conduction bands, topological state, and core levels for a series of magnetic topological insulators with stoichiometry  $\text{Mn}(\text{Bi}_{1-x}\text{Sb}_x)_2\text{Te}_4$  under the variation of the concentration of Sb atoms introduced in the process of growth in a wide range  $x = 0, 0.1, 0.2, 0.3, 0.4, 0.5$ , and 1. It has been found that the concentrations estimated from the XPS data regularly exceed the values introduced in the process of growth. It has been shown that the Dirac point is gradually shifted toward the Fermi level with an increase in the concentration of Sb atoms. The Dirac point at  $x \sim 0.3$  is localized at the Fermi level. With a further increase in the concentration of Sb atoms, the Dirac point is shifted above the Fermi level. An increase in the concentration of Sb atoms leads to the “rigid” shift of the valence band without changes in the structure of states and the fundamental band gap between the valence and conduction bands. The dependence of the shift of the Dirac point (and the entire structure of valence states) on the concentration of Sb atoms can be approximated by a square root function, which correlates with the corresponding linear increase in the charge carrier density. This behavior is characteristic of pure states of the Dirac cone at the Fermi level.

## METHODS

The ARPES and XPS measurements of the structure of the valence band and core levels were performed at one point at a temperature of 10–12 K at the UARPES setup, National Center of Synchrotron Radiation SOLARIS (Poland), at the radiation energies  $h\nu = 28$  and 120 eV, respectively. To analyze the structure of the Mn 3d level, we used the radiation energy  $h\nu = 50 \text{ eV}$  corresponding to the resonant enhancement of the intensity of the Mn 3d level. The perfectness of the crystal structure was determined by the low-energy electron diffraction method.

Additional measurements were also performed at the SPECS ProvenX-ARPES setup, Rzhhanov Institute of Semiconductor Physics, Siberian Branch, Russian Academy of Sciences (Novosibirsk), at  $h\nu = 21.22$  and 1486.7 eV for ARPES and for XPS, respectively.

Preliminary measurements were carried out at the ESCALAB 250Xi setup, Resource Center Physical Methods of Studying Surface, St. Petersburg State University.

The  $\text{Mn}(\text{Bi}_{1-x}\text{Sb}_x)_2\text{Te}_4$  single crystals were synthesized by the vertical Bridgman method at the Novosibirsk State University.

Clean surfaces of the samples were obtained by cleavage in ultrahigh vacuum. The base pressure in the experiment was  $(3-5) \times 10^{-11}$  mbar.

## ACKNOWLEDGMENTS

We are grateful to the National Center of Synchrotron Radiation SOLARIS (Poland) for access to the UARPES setup, where the measurements were performed, and to the Ministry of Education and Science of Poland (contract no. 1/SOL/2021/2, program “Support of Research and Development with the Research Infrastructure of the National Center of Synchrotron Radiation SOLARIS”). D.A. Estyunin acknowledges the support of the G-RISC program.

## FUNDING

This work was supported by the Ministry of Science and Higher Education of the Russian Federation (project no. 075-15-2020-797 (13.1902.21.0024)).

## CONFLICT OF INTEREST

The authors declare that they have no conflicts of interest.

## OPEN ACCESS

This article is licensed under a Creative Commons Attribution 4.0 International License, which permits use, sharing, adaptation, distribution and reproduction in any medium or format, as long as you give appropriate credit to the original author(s) and the source, provide a link to the Creative Commons license, and indicate if changes were made. The images or other third party material in this article are included in the article’s Creative Commons license, unless indicated otherwise in a credit line to the material. If material is not included in the article’s Creative Commons license and your intended use is not permitted by statutory regulation or exceeds the permitted use, you will need to obtain permission directly from the copyright holder. To view a copy of this license, visit <http://creativecommons.org/licenses/by/4.0/>.

## REFERENCES

1. R. Yu, W. Zhang, H.-J. Zhang, S.-C. Zhang, X. Dai, and Z. Fang, *Science* (Washington, DC, U. S.) **329**, 5987 (2010).
2. K. Nomura and N. Nagaosa, *Phys. Rev. Lett.* **106**, 166802 (2011).
3. K. He, Y. Wang, and Q.-K. Xue, *Natl. Sci. Rev.* **1**, 38 (2013).
4. C.-X. Liu, S.-C. Zhang, and X.-L. Qi, *Ann. Rev. Condens. Matter Phys.* **7**, 301 (2016).
5. J. Wang, B. Lian, and S.-C. Zhang, *Phys. Scr. T* **164**, 014003 (2015).
6. X.-L. Qi, R. Li, J. Zang, and S.-C. Zhang, *Science* (Washington, DC, U. S.) **323**, 1184 (2009).
7. R. Li, J. Wang, X.-L. Qi, and S.-C. Zhang, *Nat. Phys.* **6**, 284 (2010).
8. X. Wan, A. M. Turner, A. Vishwanath, and S. Y. Savrasov, *Phys. Rev. B* **83**, 205101 (2011).
9. W. Luo and X.-L. Qi, *Phys. Rev. B* **87**, 085431 (2013).
10. S. V. Eremeev, V. N. Men’shov, V. V. Tugushev, P. M. Echenique, and E. Chulkov, *Phys. Rev. B* **88**, 144430 (2013).
11. C.-Z. Chang, J. Zhang, X. Feng, et al., *Science* (Washington, DC, U. S.) **340**, 167 (2013).
12. M. Mogi, R. Yoshimi, A. Tsukazaki, K. Yasuda, Y. Kozuka, K. Takahashi, M. Kawasaki, and Y. Tokura, *Appl. Phys. Lett.* **107**, 182401 (2015).
13. A. M. Shikin, D. A. Estyunin, Yu. I. Surnin, A. V. Koroleva, E. V. Shevchenko, K. A. Kokh, O. E. Tereshchenko, S. Kumar, E. F. Schvier, K. Shimada, T. Yoshikawa, Y. Saitoh, Y. Takeda, and A. Kimura, *Sci. Rep.* **18**, 4813 (2019).
14. S. O. Filnov, Yu. A. Surnin, A. V. Koroleva, I. I. Klimovskikh, D. A. Estyunin, A. Yu. Varykhalov, K. A. Bokai, K. A. Kokh, O. E. Tereshchenko, V. A. Golyashov, E. V. Shevchenko, and A. M. Shikin, *J. Exp. Theor. Phys.* **129**, 404 (2019).
15. A. M. Shikin, D. A. Estyunin, A. V. Koroleva, D. A. Glazkova, T. P. Makarova, and S. O. Filnov, *Phys. Solid State* **62**, 338 (2020).
16. M. M. Otrokov, I. I. Klimovskikh, H. Bentmann, et al., *Nature* (London, U.K.) **576**, 416 (2019).
17. Y. Deng, Y. Yu, M. Z. Shi, Z. Guo, Z. Xu, J. Wang, X. H. Chen, and Y. Zhang, *Science* (Washington, DC, U. S.) **367** (6480), 895 (2020).
18. D. A. Estyunin, I. I. Klimovskikh, A. M. Shikin, E. F. Schvier, M. M. Otrokov, A. Kimura, S. Kumar, S. O. Filnov, Z. S. Aliev, M. B. Babanly, and E. V. Chulkov, *APL Mater.* **8**, 021105 (2020).
19. A. M. Shikin, D. A. Estyunin, I. I. Klimovskikh, et al., *Sci. Rep.* **10**, 13226 (2020).
20. A. M. Shikin, D. A. Estyunin, N. L. Zaitsev, et al., *Phys. Rev. B* **104**, 115168 (2021).
21. J. Zhang, C.-Z. Chang, Z. Zhang, J. Wen, X. Feng, K. Li, M. Liu, K. He, L. Wang, X. Chen, Q.-K. Xue, X. Ma, and Y. Wang, *Nat. Commun.* **2**, 574 (2011).
22. S. X. M. Riberolles, Q. Zhang, E. Gordon, N. P. Butch, L. Ke, J.-Q. Yan, and R. J. McQueeney, *Phys. Rev. B* **104**, 064401 (2021).
23. B. Chen, F. Fei, D. Zhang, et al., *Nat. Commun.* **10**, 4469 (2019).
24. X.-M. Ma, Y. Zhao, K. Zhang, et al., *Phys. Rev. B* **103**, L121112 (2021).
25. J.-Q. Yan, S. Okamoto, M. A. McGuire, A. F. May, R. J. McQueeney, and B. C. Sales, *Phys. Rev. B* **100**, 104409 (2019).
26. S. Wimmer, J. Sanchez-Barriga, P. Kupperts, et al., *Adv. Mater.* **33**, 2102935 (2021).
27. W. Ko, M. Kolmer, J. Yan, Anh D. Pham, M. Fu, F. Lupke, S. Okamoto, Z. Gai, P. Ganesh, and A.-P. Li, *Phys. Rev. B* **102**, 115402 (2020).
28. I. M. Band, Yu. I. Kharitonov, and M. B. Trzhaskovskaya, *At. Data Nucl. Data Tables* **23**, 443 (1979).
29. C. Hu, S.-W. Lien, E. Feng, S. Mackey, H.-J. Tien, I. Mazin, H. Cao, T.-R. Chang, and N. Ni, *Phys. Rev. B* **104**, 054422 (2021).
30. H. Zhang, C.-X. Liu, X.-L. Qi, X. Dai, Z. Fang, and S.-C. Zhang, *Nat. Phys.* **5**, 438 (2009).
31. H. Xie, F. Fei, F. Fang, B. Chen, J. Guo, Y. Du, W. Qi, Y. Pei, T. Wang, M. N. Saher, S. Zhang, M. Zhang, X. Wang, and F. Song, *J. Phys. D: Appl. Phys.* **55**, 104002 (2021).
32. A. M. Shikin, A. A. Rybkina, D. A. Estyunin, et al., *Sci. Rep.* **11**, 23332 (2021).

*Translated by R. Tyapaev*